


## Optomechanical Cooling and Inertial Sensing at Low Frequencies

Yanqi Zhang,<sup>1,2</sup> Adam Hines,<sup>1</sup> Dalziel J. Wilson,<sup>2</sup> and Felipe Guzman<sup>1,\*</sup>

<sup>1</sup>*Texas A&M University, Aerospace Engineering & Physics, College Station, Texas 77843, USA*

<sup>2</sup>*James C. Wyant College of Optical Sciences, University of Arizona, 1630 E. University Blvd., Tucson, Arizona 85721, USA*

 (Received 22 September 2022; revised 15 February 2023; accepted 29 March 2023; published 2 May 2023)

An inertial sensor design is proposed in this paper to achieve high sensitivity and large dynamic range in the subhertz-frequency regime. High acceleration sensitivity is obtained by combining optical cavity readout systems with monolithically fabricated mechanical resonators. A high-sensitivity heterodyne interferometer simultaneously monitors the test mass with an extensive dynamic range for low-stiffness resonators. The bandwidth is tuned by optical feedback cooling to the test mass via radiation pressure interaction using an intensity-modulated laser. The transfer gain of the feedback system is analyzed to optimize system parameters towards the minimum cooling temperature that can be achieved. To practically implement the inertial sensor, we propose a dynamic cooling mechanism to improve cooling efficiency while operating at low optical power levels. The overall system layout presents an integrated design that is compact and lightweight.

DOI: [10.1103/PhysRevApplied.19.054004](https://doi.org/10.1103/PhysRevApplied.19.054004)

### I. INTRODUCTION

Acceleration sensing is crucial for tasks such as seismology [1] and inertial navigation [2], as well as a myriad of applications spanning the automobile [3], aerospace [4], and consumer electronics industries [5]. In the past decade, advances in cavity optomechanics [6] have made it possible to develop accelerometers with ultrahigh sensitivity [7–9], relevant to tasks ranging from geodesy [10,11] to the search for gravitational wave [12,13] and dark matter [14]. Such optomechanical accelerometers typically consist of a mechanical resonator whose test mass oscillates in response to external accelerations. They also include an optical cavity to enhance the radiation pressure interaction between electromagnetic fields of light and modes of the mechanical resonator. This interaction provides high-sensitivity measurements of the test mass displacement [15]. It also provides the ability to tune the resonator frequency and damping rate via dynamic radiation pressure back-action [16,17], enabling control over the accelerometer bandwidth and dynamic range.

In the low-frequency regime (below 1 Hz), the development of high-sensitivity optomechanical accelerometers faces several challenges. The first challenge is to combine high displacement sensitivity with a large dynamic range; for resonators with low resonant frequency, the test mass displacement can reach amplitudes of hundreds to

thousands of micrometers in applications such as seismometry. In this case, cavity-enhanced readout systems such as Fabry-Perot interferometers (FPIs) are not suitable, because their dynamic range is typically lower than the optical wavelength. In addition, many noise sources exhibit  $1/f$  behavior [18] and therefore become significant at low frequencies, such as laser frequency noise [19] and thermoelastic noise [20,21]. Alternative readout systems with high dynamic range have been explored, such as the heterodyne laser interferometer proposed for the Laser Interferometry Space Antenna (LISA) and the interferometer launched in LISA Pathfinder [19,22–24]. The LISA Pathfinder interferometer (LPI) has achieved a displacement sensitivity of  $10 \text{ pm}/\sqrt{\text{Hz}}$  at 1 mHz on ground and  $30 \text{ fm}/\sqrt{\text{Hz}}$  in space. However, its assembly involves complicated alignment and bonding techniques and a bulky footprint. Recently, we developed a compact common-mode heterodyne interferometer [25–28] for inertial sensing that achieves similar sensitivity as LPIs in ground tests; however, the noise floor remains a few orders of magnitude larger than the thermal motion of the test mass, suggesting the need for a hybrid approach.

A second challenge is that lowering the resonant frequency of the mechanical resonator entails adding mass or reducing stiffness, resulting in a bulky and likely delicate system. Moreover, radiation pressure back-action damping becomes less efficient for low-frequency resonators, as it entails operating in the “bad cavity limit” [29–32], where the mechanical frequency is much smaller than the cavity bandwidth. Active radiation pressure feedback damping,

\*felipe@tamu.edu

where the test mass motion is suppressed by derivative feedback onto the laser intensity, has been demonstrated as an effective method for gram-scale resonators with mechanical frequencies of the order of 100 Hz or higher [33–36]. However, for large-mass resonators, this entails large radiation pressure forces and concomitantly high optical power-handling capacity.

In this paper, we propose an optomechanical accelerometer capable of high performance at subhertz frequencies. A key feature is the integration of two readout systems: a FPI designed for high-sensitivity displacement measurements and a heterodyne interferometer designed for high-dynamic-range displacement measurements. We show how combining these approaches with radiation pressure enables dynamic feedback cooling, a strategy whereby the resonator’s motion can be suppressed to within the linewidth of the FPI, allowing high sensitivity, high dynamic range, and reduced optical power requirements. The paper is organized as follows: in Sec. II we present the overall system design, including detailed analyses of the mechanical resonator, the optical readout systems, and the feedback cooling system; in Sec. III we describe the feedback cooling strategy and how to optimize the feedback gain to maximize cooling efficiency; Sec. IV focuses on the practical implementation of the sensor, designing the system parameters based on an optimized feedback gain. Finally, we present our dynamic feedback cooling strategy and show that it relaxes the laser power requirements while maintaining the lowest effective temperature that can be reached by the cooling process.

## II. SYSTEM DESIGN

### A. Overall system layout

The design concept for our low-frequency optomechanical inertial sensor is shown in Fig. 1. In our system, the acceleration test mass is suspended from a rigid frame, forming a mechanical oscillator. The acceleration of the frame,  $a$ , is obtained by measuring the displacement  $x$  of the test mass. The acceleration-displacement transfer function is given by the product of the oscillator (force) susceptibility  $\chi_m$  and effective mass  $m$ , namely,

$$\begin{aligned} \frac{x(\omega)}{a(\omega)} = m\chi_m(\omega) &= \frac{-1}{\omega_0^2 - \omega^2 + i(\omega\gamma_v + \omega_0^2\phi(\omega))} \\ &\equiv \frac{-1}{\omega_0^2 - \omega^2 + i\omega\gamma_m(\omega)}, \end{aligned} \quad (1)$$

where  $\omega_0$  is the resonance frequency of the test mass and  $\gamma_m(\omega) = \gamma_v + \omega_0^2\phi(\omega)/\omega$  is an effective frequency-dependent damping rate, containing a velocity damping term  $\gamma_v$  (e.g., due to gas damping), and a term  $\omega_0^2\phi(\omega)/\omega$  to internal loss in the suspension, characterized by a loss coefficient  $\phi(\omega)$  [37].

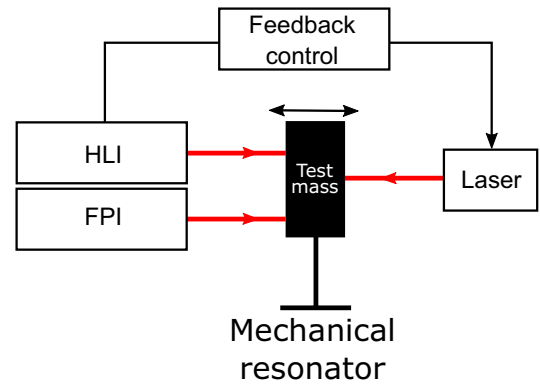


FIG. 1. Sketch of the low-frequency inertial sensor design. Two optical readout systems measure the test mass displacement at the same time. The Fabry-Perot interferometer (FPI) performs displacement measurements with high sensitivity and serves as the main optical readout system. If the test mass motion is beyond the measurement range of FPI, the resonator oscillation is cooled down by the feedback control system via radiation pressure interaction. The heterodyne laser interferometer (HLI) obtains the test mass motion and feeds into the feedback control system.

Two optical readout systems monitor the test mass displacement simultaneously. An FPI with finesse-enhanced sensitivity serves as the main readout system, and its output is converted into acceleration using Eq. (1). To address the limited tracking range of the FPI, which can only measure displacements within a range of  $\Delta x \sim \lambda$  for slower displacements than the cavity response time (Sec. II C 1) and  $\Delta x \sim \lambda/\mathcal{F}$  for faster displacements (where  $\lambda$  is the optical wavelength and  $\mathcal{F}$  is the cavity finesse), a heterodyne laser interferometer (HLI) is employed. The HLI enables simultaneous monitoring of the test mass with a significantly larger range of  $\Delta x \sim 10 \mu\text{m}$ . The purpose of the HLI is to determine whether the test mass displacement is within the FPI tracking range. If not, then the HLI output is imprinted onto the intensity of an auxiliary laser field to implement radiation pressure feedback cooling.

### B. Mechanical resonator design and characterization

The mechanical resonator, depicted in Fig. 2, consists of a 2.6-g test mass supported by a pair of flexures with 100  $\mu\text{m}$  thickness. The overall footprint is 80 mm  $\times$  90 mm and the total mass is 58.2 g. The design, optimization, and characterization of a similar mechanical resonator is discussed in detail in [37]. The monolithic resonator is fabricated of a single fused silica wafer to minimize internal losses at room temperature [38].

The thermal motion of the test mass fundamentally limits the achievable acceleration sensitivity to

$$a_{\text{th}}(\omega) = \sqrt{\frac{4k_B T}{m} \left( \gamma_v + \frac{\omega_0^2 \phi(\omega)}{\omega} \right)} \quad (2)$$

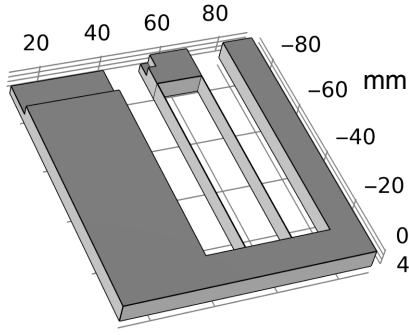


FIG. 2. Geometry of the mechanical resonator design. The 2.6-g test mass is supported by two 100- $\mu\text{m}$ -thick flexures. The overall dimension is 80 mm  $\times$  90 mm  $\times$  6.6 mm and the total mass is 58.2 g. The notch on the baseplate is designed to integrate the optical readout system, and the notch on the test mass is to mount a plane mirror.

$$= \sqrt{\frac{4k_B T \omega_0}{m} \left( \frac{1}{Q_v} + \frac{1}{Q_{\text{int}}} \frac{\omega_0}{\omega} \frac{\phi(\omega)}{\phi(\omega_0)} \right)}, \quad (3)$$

where  $k_B$  is Boltzmann's constant,  $T$  is the device temperature, and  $Q_v = \omega_0/\gamma_v$  and  $Q_{\text{int}} = \phi^{-1}(\omega_0)$  are the mechanical quality factor ( $Q$ ) due to gas damping and the internal friction, respectively.

Equation (2) shows that a large  $mQ/\omega_0$  factor is desirable to reduce thermal noise. To determine the resonance frequency  $\omega_0$  and estimate the internal  $Q$ , we conducted ringdown measurements at a vacuum pressure of 10  $\mu\text{Torr}$  (to minimize gas damping,  $\gamma_v$ ) in [10]. The ringdown for a device with  $\omega_0 = 2\pi \times 4.72$  Hz yielded  $Q = 4.77 \times 10^5$ , a  $mQ$  product of 1240 kg, corresponding to an acceleration noise floor of  $a_{\text{th}}(\omega_0) = 1 \times 10^{-11} \text{ m s}^{-2}/\sqrt{\text{Hz}}$  near resonance [10] and a baseband thermal displacement of  $x_{\text{th}}(\omega \ll \omega_0) = \omega_0^{-2} a_{\text{th}}(\omega) \approx 1 \times 10^{-14} \text{ m}/\sqrt{\text{Hz}}$ .

### C. Optical readout systems

#### 1. Fabry-Perot interferometer

For our main optical readout system, we envision a FPI of  $L \approx 50$  mm, formed by mounting one mirror onto the test mass and the other onto the resonator frame. A shorter ( $L \sim 100$   $\mu\text{m}$ ) fiber-mirror-based cavity was previously demonstrated for a stiffer (10-kHz) version of our resonator [8]; in this case the large motion of our 5-Hz test mass requires a free space approach. The cavity finesse is designed to be  $\mathcal{F} \approx 600$ , equivalent to the reflectance  $R \approx 99.5\%$  for both cavity mirrors. The cavity displacement readout is conducted by measuring the frequency fluctuations of a  $\lambda = 1064$  nm laser, envisioned to be frequency-locked to a FPI resonance using the Pound-Drever-Hall (PDH) technique [39,40]. The absolute laser frequency is meanwhile tracked by beating it against an iodine-referenced laser or another suitable optical frequency reference. Within the bandwidth of the

laser-cavity lock, the cavity length  $L$  and laser frequency  $\nu$  fluctuations are related by

$$\frac{d\nu}{dL} = \frac{\nu}{L} = \frac{c}{\lambda L}. \quad (4)$$

The readout signal can, thus, be expressed as

$$\nu(\omega) = \frac{c}{\lambda L} (x_{\text{ext}}(\omega) + x_{\text{th}}(\omega) + x_n(\omega)) \quad (5a)$$

$$= \frac{c}{\lambda L} \frac{a_{\text{ext}}(\omega) + a_{\text{th}}(\omega) + a_n(\omega)}{\omega_0^2 - \omega^2 + i(\omega\gamma_v + \omega_0^2\phi(\omega))}, \quad (5b)$$

where  $a_{\text{ext}}$  ( $x_{\text{ext}}$ ) is the acceleration (displacement) signal and  $a_n$  ( $x_n$ ) is the apparent acceleration (displacement) due to readout noise. We note that our target sensitivity,  $x_n \sim x_{\text{th}} \approx 10^{-14} \text{ m}/\sqrt{\text{Hz}}$ , is modest for a quantum-limited PDH measurement ( $x_n \propto \lambda/\mathcal{F}^2 P_{\text{in}}$  [41]), and was surpassed by two orders of magnitude by our earlier fiber cavity with  $\mathcal{F} = 1600$  and an input power of  $P_{\text{in}} = 1$  mW [8]. The main challenge is the laser frequency noise requirement,  $(c/\lambda L)x_{\text{th}} \approx 60$  Hz, which we envision meeting with an actively stabilized Nd:YAG laser [42].

An important limitation of the FPI is its tracking range. For sufficiently slow changes, the largest measurable test mass displacement  $\Delta x$  is related to the laser frequency tuning range  $\Delta\nu$ , namely,

$$\Delta x = \frac{\lambda L}{c} \Delta\nu \quad (6a)$$

$$= 1.8 \mu\text{m} \times \frac{\Delta\nu}{10 \text{ GHz}} \frac{\lambda}{1064 \text{ nm}} \frac{L}{50 \text{ mm}}. \quad (6b)$$

In Eq. (6b) we estimate  $\Delta x = 1.8 \mu\text{m}$  for a typical commercial Nd:YAG laser with a tuning range of 10 GHz. We anticipate that this dynamic range will be too small for operation in a nonisolated environment because it is equivalent to a resonant acceleration noise of only  $\Delta x \omega_0/\sqrt{Q} \approx 8 \text{ ng}/\sqrt{\text{Hz}}$ . With this in mind, in the following sections, we propose a HLI to monitor the full range of the test mass motion and radiation-pressure feedback damp the motion using the HLI output as an error signal.

#### 2. Long-range HLI

Heterodyne interferometry is a common measurement technique that can achieve high sensitivity, large dynamic range, and traceable calibration. Recently, we developed a compact HLI [27] for use with low-frequency optomechanical inertial sensing. Our HLI employs a common-path design, as shown in Fig. 3, to provide a high rejection ratio to various forms of environmental noise.

Concretely, a measurement interferometer (MIFO) measures the test mass motion and a reference interferometer (RIFO) of common optical paths with MIFO monitors ambient noise. The RIFO signal is then subtracted from

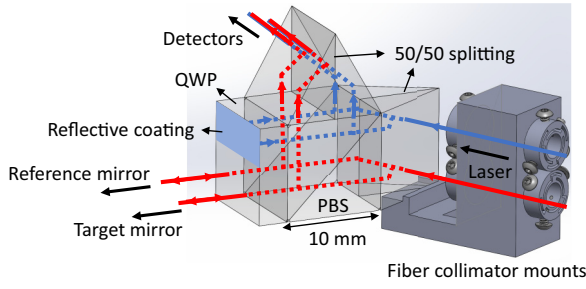


FIG. 3. Schematic diagram of the quasi-monolithic interferometer unit in the isometric view. Two incoming laser beams are split into four beams by the 50:50 nonpolarizing splitting surface embedded in the equilateral triangular prism. The beam pair with different frequencies constructs one interferometer. The measurement interferometer (MIFO) measures the target displacement. The reference interferometer (RIFO) measures systematic noises that share the common optical paths with the MIFO. The target displacement is calculated from the difference between MIFO and RIFO measurements.

the MIFO output to reduce its noise content. The complete system has a footprint of  $20 \text{ mm} \times 20 \text{ mm} \times 10 \text{ mm}$  and weighs 4.5 g. To achieve such a compact assembly, all the optical components are cemented as a quasi-monolithic unit. The small size and weight enable integration onto the mechanical resonator's frame. Preliminary tests have yielded a noise floor of  $2 \times 10^{-13} \text{ m}/\sqrt{\text{Hz}}$  around 1 Hz, limited by photodetector noise, as shown in Fig. 4[27]. If the displacement recorded by the HLI is outside the dynamic range of the FPI, the HLI data are used as the error signal of the feedback control system described in the next section.

#### D. Feedback control system

The feedback control system includes signal processing modules and digital-analog converters to actuate the test mass. Minimal contact with the test mass is desirable to reduce surface losses. We therefore consider radiation pressure as a feedback actuator. An advantage of this approach is the traceability of the radiation pressure force through the laser wavelength [43,44].

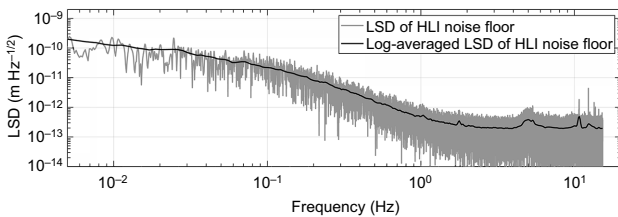


FIG. 4. Linear spectral density (LSD) and its logarithmic average of the heterodyne laser interferometer (HLI) [27] noise floor. The interferometer prototype shows a noise floor of  $2 \times 10^{-13} \text{ m}/\sqrt{\text{Hz}}$  above 1 Hz when tested in vacuum.

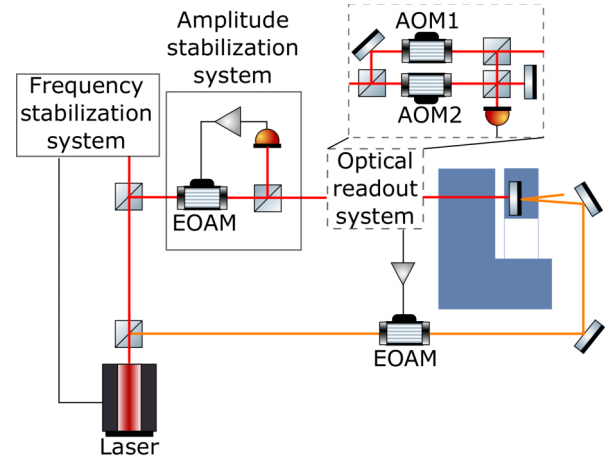


FIG. 5. Layout of the feedback control system. The feedback force is provided by radiation pressure interaction between an intensity-modulated laser beam and the test mass. The laser intensity is modulated by an electro-optical amplitude modulator (EOAM). The displacement of the test mass is read out by a heterodyne interferometer (simplified in the figure), and sent to the feedback control loop. The controller in the feedback loop calculates and outputs a corresponding voltage signal to the EOAM to modulate actuating laser intensity. The laser is stabilized in frequency and amplitude to reduce the measurement noise.

Figure 5 shows our proposed radiation pressure feedback scheme, employing an auxiliary laser beam, reflected off the test mass, whose intensity is modulated with a filtered copy of HLI photosignal. To control the test mass position  $x$  in a traceable manner, it is necessary to understand the transduction chain comprising the feedback circuit. To this end we consider the model

$$\begin{aligned} x(\omega) &= \chi_m(\omega)(F_{\text{th}}(\omega) + F_{\text{ext}}(\omega) + F_{\text{fb}}(\omega)) \\ &= \chi_m(\omega)(F_{\text{th}}(\omega) + F_{\text{ext}}(\omega) - \chi_{\text{fb}}(\omega)y(\omega)) \\ &= \chi_{\text{eff}}(\omega)(F_{\text{th}}(\omega) + F_{\text{ext}}(\omega) - \chi_{\text{fb}}(\omega)x_n(\omega)), \end{aligned} \quad (7)$$

where  $y = x + x_n$  is the apparent displacement detected by the HLI, with readout noise  $x_n$ ,  $F_{\text{fb}}$  is the radiation pressure feedback force,  $\chi_{\text{fb}}(\omega) \equiv -F_{\text{fb}}(\omega)/y(\omega)$  is the feedback gain, and

$$\chi_{\text{eff}}(\omega) \equiv \frac{\chi_m(\omega)}{1 + \chi_m(\omega)\chi_{\text{fb}}(\omega)} \quad (8)$$

is the effective (closed-loop) mechanical susceptibility.

It is evident from Eq. (7) that the thermal force sensitivity remains unchanged by the feedback actuation; however, as shown in the following, feedback damping ( $\chi_{\text{fb}} \propto i\dot{x}$ ) is advantageous because it allows the sensor to operate in the linear regime  $x \ll \lambda/\mathcal{F}$ , by reducing the displacement on resonance. The cost of this extended dynamic range is additional stochastic force due to the feedback of measurement noise,  $\chi_{\text{fb}}(\omega)x_n(\omega)$ .

The phase and magnitude of the feedback gain must be tailored to achieve a desired closed-loop response and noise figure, which can be tailored in the digital loop software. We thus consider the following model for the feedback gain

$$\chi_{\text{fb}}(\omega) = G_{FP} G_{PV} G_{Vx}(\omega), \quad (9)$$

where  $G_{FP}$  and  $G_{PV}$  are the steady-state response functions of the radiation pressure actuator and intensity modulator, respectively, and  $G_{Vx}(\omega)$  is the frequency dependent response function of the software-interfaced HLI that considers the digital processing for phase extraction (phasemeter).

To model the actuator transfer function, we assume the test mass has perfect reflectivity for the power  $P$  incident on the test mass. Thus, we obtain

$$G_{FP} = \frac{dF_{\text{RP}}}{dP} = \frac{2}{c}. \quad (10)$$

The transfer function of the intensity modulator depends on the modulation method. We envision an intensity modulator based on a polarization-based EOAM, for which the output power  $P$  (referred to the power incident on the test mass) is related to the voltage  $V$  applied across the electrodes as  $P = P_0 \cos^2(\pi V/V_\pi)$ , where  $P_0$  is the maximum transmitted power and  $V_\pi$  is the half-wave voltage of the EOAM. This leads to a transfer function

$$G_{PV} = \frac{dP}{dV} = \frac{\pi P_0 \sin(V/V_\pi)}{V_\pi}. \quad (11)$$

Finally, the transfer function of the HLI depends on the phase measurement technique. Common phase extraction algorithms include phase-locked loop (PLL) [45] and single-bin DFT algorithms [19]. A disadvantage of these methods is that both involve computationally intensive inverse trigonometric functions, which lead to a nonlinear time-invariant (NLTI) system. Instead, we propose a digital phasemeter, which only requires a low-pass filter. The phase response of the entire system is determined by this filter, and has a negligible effect at low frequencies. With this assumption, the HLI transfer function  $G_{Vx}$  can be expressed as

$$G_{Vx}(\omega) = \frac{V(\omega)}{x(\omega)} = G_{\text{DAC}}(\omega) \frac{2\pi}{\lambda}, \quad (12)$$

where  $G_{\text{DAC}}$  is a (complex-valued) gain that can be set when converting the measured phase to the analog voltage output applied to the EOAM. The significance of  $G_{\text{DAC}}$  is explained in detail in Sec. IV A.

Combining Eqs. (9)–(12), the feedback gain of the system shown in Figure 5, can be expressed as

$$\chi_{\text{fb}}(\omega) \approx \frac{4\pi^2}{c\lambda} \frac{G_{\text{DAC}}(\omega) P_0 \sin 2\theta}{V_\pi}, \quad (13)$$

where system parameters such as the laser power  $P_0$  can be optimized to enhance the feedback cooling efficiency.

### III. FEEDBACK COOLING OPTIMIZATION

#### A. Optical cooling

In feedback cooling protocols, derivative feedback gain (i.e., a velocity-proportional feedback force) is used to damp the test mass displacement  $x$  to the measurement noise floor  $x_n$ . Although at high frequencies it is customary to approximate derivative gain over a narrow band of frequencies near resonance [46], for our low-frequency system ( $< 10$  Hz), digital filtering can provide a good approximation to analog derivative control extending to baseband. We thus consider the following derivative feedback gain model [46]

$$\chi_{\text{fb}}(\omega) = \text{img} \gamma_m(\omega) \omega, \quad (14)$$

where  $g$  is a unitless gain factor.

Following Eq. (8), the closed-loop mechanical susceptibility becomes

$$\chi_{\text{eff}}(\omega) = \frac{1}{m[\omega_0^2 - \omega^2 + i(1+g)\gamma_m(\omega)\omega]} \quad (15a)$$

$$\equiv \frac{1}{m[\omega_0^2 - \omega^2 + i\gamma_{\text{eff}}(\omega)\omega]}, \quad (15b)$$

which is characterized by an effective damping rate  $\gamma_{\text{eff}}(\omega) \equiv (1+g)\gamma_m(\omega)$ .

#### B. Feedback gain optimization

Figure 6 suggests that increasing the feedback gain  $g$  reduces the test mass displacement at resonance. However, it also increases the feedback of the measurement noise, expressed by the term  $\chi_{\text{fb}} x_n$  in Eq. (7). As a result, there is an optimal gain at which the total closed-loop displacement can be minimized. This can be seen by rewriting Eq. (7) in terms of the closed-loop displacement power spectral density

$$S_{xx}(\omega) = |\chi_{\text{eff}}(\omega)|^2 (S_{FF}^{\text{th}}(\omega) + S_{FF}^{\text{ext}}(\omega) + |\chi_{\text{fb}}(\omega)|^2 S_{xx}^n(\omega)) \quad (16)$$

and integrating over the resonance peak to give the closed-loop displacement variance

$$\langle x^2 \rangle \approx \frac{1}{1+g} \langle x_{\text{th},0}^2 \rangle + \frac{g^2}{1+g} \langle x_n^2 \rangle + \langle x_{\text{ext}} \rangle^2 (g) \quad (17)$$

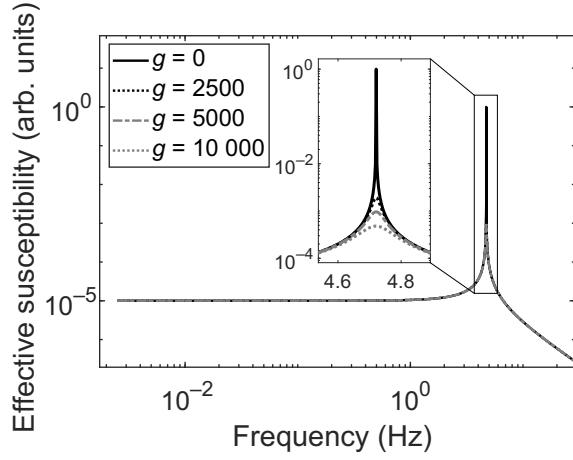


FIG. 6. Effective susceptibility  $\chi_{\text{eff}}(\omega)$  of the test mass for different gain factors  $g = 0, 2500, 5000,$  and  $10000$ . The case of  $g = 0$  represents the open-loop mechanical susceptibility. Increasing  $g$  reduces driven displacement on resonance.

where  $\langle x_{\text{th},0}^2 \rangle = k_B T / m\omega_0^2 \approx \gamma_m S_{xx}^{\text{th}}(\omega_0) / 4$  is the open-loop thermal displacement,  $\langle x_n^2 \rangle \approx \gamma_m S_{xx}^n(\omega_0) / 4$  is the apparent displacement due to measurement noise, and  $\langle x_{\text{ext}}^2 \rangle = \int |\chi_{\text{eff}}(\omega)|^2 S_{FF}^{\text{ext}}(\omega) d\omega / 2\pi$  is the closed-loop displacement due to external forces.

In principle,  $g$  can be tailored to minimize  $\langle x^2 \rangle$  (note that, in general,  $\langle x_{\text{ext}}^2 \rangle(g > 0) \leq \langle x_{\text{ext}}^2 \rangle(0)$ ); however, the magnitude of this gain depends on the external force spectrum  $S_{FF}^{\text{ext}}(\omega)$ . Without knowing  $S_{FF}^{\text{ext}}(\omega)$ , it is customary to optimize  $g$  to minimize the thermal noise, i.e.,

$$g_{\text{opt}} \approx \sqrt{\frac{\langle x_{\text{th},0}^2 \rangle}{\langle x_n^2 \rangle}} = \sqrt{\frac{4k_B T}{m\omega_0^2 \gamma_m S_{xx}^n}}, \quad (18)$$

yielding

$$\langle x^2 \rangle_{\text{min}} \geq 2\sqrt{\langle x_{\text{th},0}^2 \rangle \langle x_n^2 \rangle} \quad (19)$$

in the limit  $g_{\text{opt}} \gg 1$  (corresponding to a large open-loop thermal-to-measurement-noise ratio). The effect of this feedback strategy is to reduce the effective temperature of the test mass vibration to

$$T_{\text{eff}} = \frac{m\omega_0^2 \langle x^2 \rangle}{k_B} \geq \frac{1}{1+g} T + \frac{g^2}{1+g} T_n \geq 2\sqrt{TT_n}, \quad (20)$$

where  $T_n \equiv m\omega_0^2 \langle x_n^2 \rangle / k_B$  is the apparent temperature of the readout noise and the minimal value is obtained for  $g = g_{\text{opt}}$  in the absence of external forces.

Finally, we note that at  $g = g_{\text{opt}}$ , the added force noise  $|\chi_{\text{fb}}|^2 S_{xx}^n$  is commensurate with thermal noise  $S_{FF}^{\text{th}}$ , resulting in a two-fold reduction in force sensitivity at frequencies where thermal motion  $S_{xx}^{\text{th}}$  dominates the open-loop displacement measurement, and negligible change

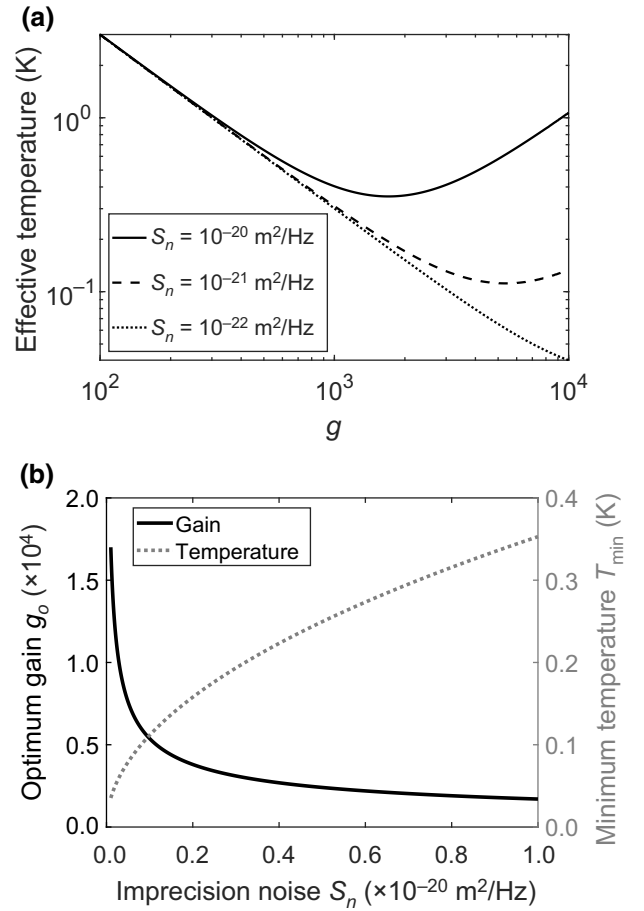


FIG. 7. (a) Relation between effective temperature and gain factor for different levels of readout imprecision noise. (b) Minimum temperature that the cooling system can achieve and the corresponding gain factor to achieve this temperature versus the readout imprecision noise in the system.

where readout noise  $S_{xx}^n$  dominates. Practically, the latter corresponds to baseband frequencies ( $\omega \ll \omega_0$ ) where acceleration sensing is carried out.

In Fig. 7(a), we plot the effective temperature of the resonator described in Sec. II B, subject to feedback cooling with a variety of gains and measurement noise levels, assuming  $T = 300$  K. In Fig. 7(b) we plot the optimal gain and associated minimal temperature as a function of measurement noise. In the next section we consider a parameter space that is practically accessible.

#### IV. FEEDBACK IMPLEMENTATION

In this section, we consider how to practically implement feedback cooling of our low-frequency resonator, described in Sec. II B [10]. We are particularly interested in the requirements to cool the test mass to the measurement noise floor, corresponding to a gain factor of  $g = g_{\text{opt}}$  [Eq. (18)]. Building upon the recent development of a monolithic HLI integrated with a similar test mass [26], we

conservatively assume  $\sqrt{S_{xx}^n} = 5 \times 10^{-12} \text{ m}/\sqrt{\text{Hz}}$ . Combined with the test mass properties described in Sec. II B, this implies  $g_{\text{opt}} = 3.40 \times 10^4$ . We find that achieving this gain factor is challenging with the long-range (HLI) detection scheme, due to its (deliberately) small transduction gain. To overcome this challenge, we propose a dynamic gain feedback cooling strategy employing both long-range (HLI) and high-sensitivity (FPI) readout systems in series.

### A. System parameters

Combining Eqs. (13) and (14), near the resonance frequency, the feedback gain factor  $g$  is related to the system parameters in the control loop by

$$g = |\chi_{\text{fb}}(\omega_0)| \frac{Q}{m\omega_0^2} = \frac{4\pi^2}{c\lambda} \frac{Q}{m\omega_0^2} \frac{|G_{\text{DAC}}(\omega_0)| P_0 \sin 2\theta}{V_\pi}. \quad (21)$$

In practice, the EOAM phase is adjusted to maximize the modulation depth, corresponding to  $\sin 2\theta = 1$ . The remaining free parameters are the optical power  $P_0$ , the half-wave voltage  $V_\pi$ , and the (complex-valued) digital conversion gain  $G_{\text{DAC}}$ , which is the parameter that provides the largest tuning range.

As mentioned in Sec. II D, the digital gain,  $G_{\text{DAC}}$ , is a complex variable factor in the digital-to-analog conversion (DAC) coefficient that translates the digital phasemeter output, a phase in radians, into a corresponding proportional analog voltage that is injected into the EOAM to control the optical power used for feedback cooling. In practice, the magnitude of  $G_{\text{DAC}}$  is limited by the EOAM half-wave voltage ( $V_\pi$ ) and the physical displacement range of the test mass  $x_{p-p}$ , where

$$|G_{\text{DAC}}^{\text{max}}| = \frac{V_\pi \lambda}{2\pi x_{p-p}}. \quad (22)$$

### B. Feedback cooling with HLI detector

The open-loop displacement of our test mass has been measured to be of the order of  $\pm 100 \mu\text{m}$  in our laboratory, without vibration isolation. Combining Eqs. (18), (21), and (22), with the mechanical properties of the resonator in Sec. II B, we predict that the minimum laser power  $P_0$  needed to achieve a gain factor  $g = 1$  ( $T_{\text{eff}} = T/2$ ) is 1.16 mW, and the laser power to achieve  $g_{\text{opt}} = 3.40 \times 10^4$  is 34.43 W. Thus, we find that, for our current test mass, feedback cooling with the long-range HLI detector is challenging due to the required high laser power. In particular,  $P_0 \gtrsim 100 \text{ mW}$  has the potential to damage the EOAM crystal. It also poses a challenge in terms of thermal management and handling of other components in the system such as the fiber couplers and photodetectors. To reduce the power requirements, we propose a dynamic

cooling mechanism employing a dynamical gain  $G_{\text{DAC}}$ , as discussed in the following.

### C. Dynamic feedback cooling

The critical factor limiting the single-stage cooling approach is the readout conversion coefficient  $G_{\text{DAC}}$ . To overcome this limitation, we can use the fact that the maximum gain,  $G_{\text{DAC}}^{\text{max}}$ , can be increased as the test mass is cooled, allowing for use of less optical power. This means that we can *dynamically* increase  $G_{\text{DAC}}$  as the oscillation amplitude of the test mass goes down. In fact, we can also dynamically switch from the low-sensitivity HLI readout scheme to the high-sensitivity FPI readout scheme when the test mass oscillation is suppressed to  $\sqrt{\langle x^2 \rangle} < \lambda/\mathcal{F}$ . The trade-off of this dynamic gain approach is that it takes time for the oscillator to relax to a steady state between gain settings. Specifically, the displacement variance decays as [47]

$$\langle x^2(t) \rangle = \frac{\langle x^2(0) \rangle}{1+g} (1 + g \exp^{-(1+g)\gamma_m t}), \quad (23)$$

where  $\gamma_m \sim 2\pi \cdot 10 \mu\text{Hz}$  is the open-loop damping rate.

In Fig. 8 we present simulations of single-step and dynamic feedback cooling of our test mass for various gain settings and optical powers, using the HLI detector and system parameters described previously. Relative to single-step cooling with  $P_0 \approx 34 \text{ W}$ , dynamic cooling enables optimal gain ( $g_{\text{opt}} = 3.4 \times 10^4$ ) to be reached with  $10^4$ -fold lower optical power ( $P_0 \approx 1 \text{ mW}$ ), at the expense of a  $10^4$ -fold longer cooling time (10 days, versus 1 min). We emphasize that an optical power of  $P_0 = 1 \text{ mW}$  is sufficient to counteract the thermal motion of our 2.5 g test mass, because the associated radiation pressure force,  $F_{\text{RP}} = 2P/c = 7 \times 10^{-12} \text{ N}$ , is four orders of magnitude larger than the root-mean-squared thermal force integrated over the mechanical bandwidth,  $\Delta F_{\text{th}} = \sqrt{8\pi k_B T m} \times (f/Q) = 2 \times 10^{-16} \text{ N}$ . This counterintuitive result is a consequence of the ultralow damping rate,  $f/Q \sim 10 \mu\text{Hz}$ , of the test mass vibration.

As shown in Fig. 9, the total cooling time for the dynamic approach depends on the initial gain factor  $g_0$ , which is proportional to optical power, and scales approximately inversely with  $g_0$ . In practice, however, we can cool the test mass down to within the FPI capture range at much lower gains than  $g_{\text{opt}}$ , which allows us to switch to a FPI readout much faster. In this case, the required time in our dynamic cooling approach can be reduced to a few hours using an optical power feedback of only 11.59 mW, as shown in Fig. 9.

## V. COMPLETE SYSTEM OVERVIEW

The complete system we propose is shown in Fig. 10, including the dual measurement scheme and radiation

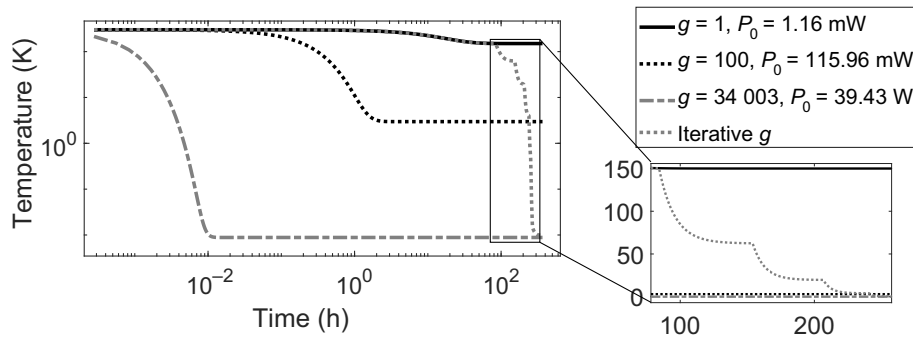


FIG. 8. Effective temperature of the test mass subject to feedback cooling with a constant gain factor  $g = 1$ ,  $100$ , and  $3.40 \times 10^4$ , and for an iteratively increased  $g$  (dynamic feedback cooling). Each step on the iterative curve corresponds to the moment when  $G_{\text{DAC}}$  changes. The inset shows an enlarged view of the final state for  $g = 100$  and  $3.40 \times 10^4$ , and the iterative  $g$ . In the dynamic cooling mechanism, the initial gain factor is  $g_0 = 1$ . After six iterations, its final state reaches the same level as single-step feedback cooling with  $g_{\text{opt}} = 3.40 \times 10^4$ . For iterative cooling, the optical power is fixed at  $P_0 = 1.16$  mW.

pressure feedback circuit. In this figure we show three lasers for simplicity, however, we note that all these three sources can be obtained from a single laser unit, following a proper optical setup and frequency management. The three optical sources are: (a) the frequency-stabilized laser that serves as the optical source for the heterodyne interferometer to monitor the full-range motion of the test mass, as well as the frequency standard to obtain the frequency drift of the probe laser; (b) the probe laser, which is the optical source for the FPI, allowing for high-sensitivity displacement measurements; and (c) the feedback laser, which is interfaced with an EOAM intensity modulator for feedback cooling.

The feedback circuit is shown at the top right of Fig. 10. For simplicity, we omit the fact that the HLI output passes through a near-resonant bandpass filter and a phase shifter in this Figure, to avoid crosstalk from higher-order modes as well as to provide a  $90^\circ$  phase shift for the feedback

force, respectively. The optical components of both the heterodyne interferometer and the FPI can be mounted on the resonator frame, leading to a compactly integrated and vacuum-compatible inertial sensor. This design also reduces the effect of mechanical vibrations and thermal expansion, which are significant noise sources at low frequencies.

In closed loop, the detected laser frequency fluctuations in Eq. (5b) can be rewritten as

$$\Delta\nu = \frac{c}{\lambda L} \frac{a_{\text{ext}}(\omega) + a_{\text{th}}(\omega) + a_n(\omega)}{\omega_0^2 - \omega^2 + i(1+g)\omega\omega_0/Q}, \quad (24)$$

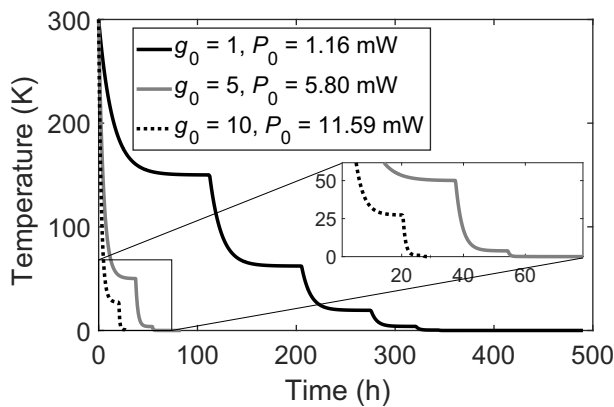


FIG. 9. Effective temperature in a dynamic cooling mechanism for different initial gain factors  $g_0 = 1$ ,  $5$ , and  $10$ . A large  $g_0$  allows the system to operate much faster and with fewer iterations to achieve a certain final state.

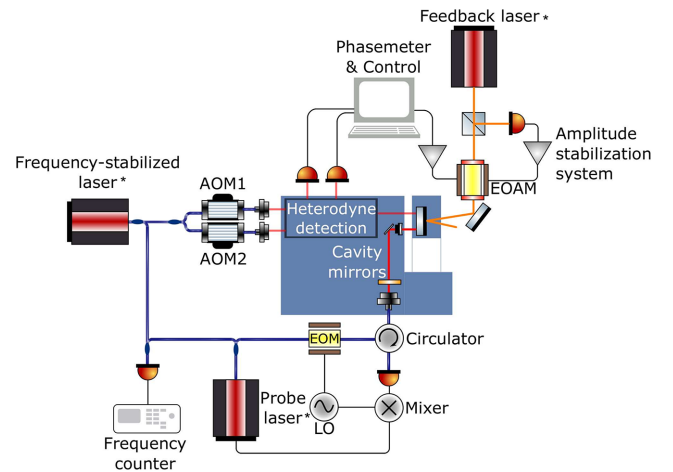


FIG. 10. Overall layout of the optomechanical inertial sensor design, including details of the mechanical resonator, the optical readout systems, and the feedback control system. Three individual lasers are used in this figure due to their different purposes in the system. Note that, in practice, all three lasers can be replaced with a single laser source, following a proper optical setup and frequency management.



where  $g$  in the dynamic cooling system can be traced to the final  $G_{\text{DAC}}$  via Eq. (21). All the parameters in Eq. (24), such as  $\omega_0$ ,  $Q$ ,  $\bar{\lambda}$ , and  $\bar{L}$  can be measured directly and independently from the displacement sensitivity measurement.

## VI. CONCLUSIONS AND OUTLOOK

We have proposed an optomechanical inertial sensor that features high displacement sensitivity, to enable thermal-noise-limited performance, and the ability to perform large-amplitude acceleration measurements in non-isolated environments via radiation pressure feedback cooling. The design principles are described in detail for each subsystem, followed by a discussion of a practical implementation. A novel dynamic cooling approach is presented, which reduces the laser power requirements and improves the cooling efficiency.

Dynamic feedback cooling of our relatively large, low-frequency test mass allows the use of low optical power, at the milliwatt level. However, this feature comes at the expense of prolonging the time needed for the optical cooling process, when compared with a single-step method that utilizes high laser power (tens of watts). Nonetheless, this extended time in reaching the minimal operational resonator temperature may likely be acceptable for applications where the sensor is deployed permanently, and the dynamic cooling is part of the initial calibration process. Seismic monitoring of a particular site or space missions are examples of such applications, because they typically require commissioning of their instrumentation over comparable time scales. Our design thus introduces a promising optomechanical inertial sensing technology that is capable of reaching high acceleration sensitivity at low frequencies (below  $1 \times 10^{-9} \text{ m s}^{-2}/\sqrt{\text{Hz}}$  above 1 mHz [10]). This system is currently under development in our laboratory.

## ACKNOWLEDGMENTS

The authors acknowledge financial support from the National Science Foundation (NSF) through grants PHY-2045579, PHY-2209473, and ECCS-1945832, and the National Aeronautics and Space Administration (NASA) through grant 80NSSC20K1723.

- 
- [1] M. S. Hons, PhD Thesis, University of Calgary, Department of Geoscience, 2008.  
 [2] N. Yazdi, F. Ayazi, and K. Najafi, Micromachined inertial sensors, *Proc. IEEE* **86**, 1640 (1998).  
 [3] S. Finkbeiner, in *2013 Proceedings of the European Solid-State Device Research Conference (ESSDERC)* (IEEE, Bucharest, Romania, 2013), p. 9.

- [4] M. Schmitz, A. Leister, N. Dezfuli, J. Riemann, F. Müller, and M. Mühlhäuser, in *Proceedings of the 2016 CHI Conference Extended Abstracts on Human Factors in Computing Systems, CHI EA '16* (Association for Computing Machinery, New York, NY, USA, 2016), p. 2688.  
 [5] W. Babatain, S. Bhattacharjee, A. M. Hussain, and M. M. Hussain, Acceleration sensors: Sensing mechanisms, emerging fabrication strategies, materials, and applications, *ACS Appl. Electron. Mater.* **3**, 504 (2021).  
 [6] M. Aspelmeyer, T. J. Kippenberg, and F. Marquardt, Cavity optomechanics, *Rev. Mod. Phys.* **86**, 1391 (2014).  
 [7] A. G. Krause, M. Winger, T. D. Blasius, Q. Lin, and O. Painter, A high-resolution microchip optomechanical accelerometer, *Nat. Photonics* **6**, 768 (2012).  
 [8] F. Guzman, L. Kumanchik, J. Pratt, and J. M. Taylor, High sensitivity optomechanical reference accelerometer over 10 kHz, *Appl. Phys. Lett.* **104**, 221111 (2014).  
 [9] F. Zhou, Y. Bao, R. Madugani, D. A. Long, J. J. Gorman, and T. W. LeBrun, Broadband thermomechanically limited sensing with an optomechanical accelerometer, *Optica* **8**, 350 (2021).  
 [10] A. Hines, A. Nelson, Y. Zhang, G. Valdes, J. Sanjuan, J. Stoddart, and F. Guzmán, Optomechanical accelerometers for geodesy, *Remote Sens.* **14**, 4389 (2022).  
 [11] K. Abich, *et al.*, In-Orbit Performance of the GRACE Follow-on Laser Ranging Interferometer, *Phys. Rev. Lett.* **123**, 031101 (2019).  
 [12] A. Bertolini, *High Sensitivity Accelerometers For Gravity Experiments* (Citeseer, Pisa, Italy, 2001).  
 [13] J. Van Heijningen, A. Bertolini, and J. F. van den Brand, in *2018 IEEE Sensors Applications Symposium (SAS)* (IEEE, Seoul, Korea (South), 2018), p. 1.  
 [14] D. Carney, A. Hook, Z. Liu, J. M. Taylor, and Y. Zhao, Ultraviolet dark matter detection with mechanical quantum sensors, *New J. Phys.* **23**, 023041 (2021).  
 [15] V. B. Braginskii and A. B. Manukin, *Measurement of weak forces in physics experiments*, edited by David H. Douglass (University of Chicago Press, Chicago, 1977).  
 [16] B. S. Sheard, M. B. Gray, C. M. Mow-Lowry, D. E. McClelland, and S. E. Whitcomb, Observation and characterization of an optical spring, *Phys. Rev. A* **69**, 051801 (2004).  
 [17] T. Corbitt, D. Ottaway, E. Innerhofer, J. Pelc, and N. Mavalvala, Measurement of radiation-pressure-induced optomechanical dynamics in a suspended Fabry-Perot cavity, *Phys. Rev. A* **74**, 021802 (2006).  
 [18] B. J. West and M. F. Shlesinger, On the ubiquity of  $1/f$  noise, *Int. J. Mod. Phys. B* **3**, 795 (1989).  
 [19] G. Heinzel, V. Wand, A. García, O. Jennrich, C. Braxmaier, D. Robertson, K. Middleton, D. Hoyland, A. Rüdiger, R. Schilling, U. Johann, and K. Danmann, The LTP interferometer and phasemeter, *Classical Quantum Gravity* **21**, S581 (2004).  
 [20] M. Nofrarias, F. Gibert, N. Karnesis, A. F. Garcia, M. Hewitson, G. Heinzel, and K. Danzmann, Subtraction of temperature induced phase noise in the LISA frequency band, *Phys. Rev. D* **87**, 102003 (2013).  
 [21] F. Gibert, *et al.*, Thermo-elastic induced phase noise in the LISA Pathfinder spacecraft, *Classical Quantum Gravity* **32**, 045014 (2015).  
 [22] S. M. Aston and C. C. Speake, in *Laser Interferometer Space Antenna: 6th International LISA Symposium*,

- American Institute of Physics Conference Series, Vol. 873, edited by S. M. Merkovitz and J. C. Livas (AIP, Greenbelt, USA, 2006), p. 326.
- [23] T. Schuldt, H.-J. Kraus, D. Weise, C. Braxmaier, A. Peters, and U. Johann, in *Society of Photo-Optical Instrumentation Engineers (SPIE) Conference Series*, Society of Photo-Optical Instrumentation Engineers (SPIE) Conference Series, Vol. 6293 (SPIE, San Diego, USA, 2006), p. 62930Z.
- [24] F. Guzman, Ph.D. dissertation, Max Planck Institute for Gravitational Physics & Gottfried Wilhelm Leibniz Universität Hannover, Hannover, Germany, 2009.
- [25] K.-N. Joo, E. Clark, Y. Zhang, J. D. Ellis, and F. Guzmán, A compact high-precision periodic-error-free heterodyne interferometer, *J. Opt. Soc. Am. A* **37**, B11 (2020).
- [26] Y. Zhang, A. Hines, G. Valdes, and F. Guzman, Investigation and mitigation of noise contributions in a compact heterodyne interferometer, *Sensors* **21**, 5788 (2021).
- [27] Y. Zhang and F. Guzman, Quasi-monolithic heterodyne laser interferometer for inertial sensing, *Opt. Lett.* **47**, 5120 (2022).
- [28] Y. Zhang and F. Guzman, Fiber-based two-wavelength heterodyne laser interferometer, *Opt. Express* **30**, 37993 (2022).
- [29] V. Braginsky, S. Strigin, and S. Vyatchanin, Parametric oscillatory instability in Fabry-Perot interferometer, *Phys. Lett. A* **287**, 331 (2001).
- [30] O. Arcizet, P.-F. Cohadon, T. Briant, M. Pinard, and A. Heidmann, Radiation-pressure cooling and optomechanical instability of a micromirror, *Nature* **444**, 71 (2006).
- [31] S. Gigan, H. R. Böhm, M. Paternostro, F. Blaser, G. Langer, J. B. Hertzberg, K. C. Schwab, D. Bäuerle, M. Aspelmeyer, and A. Zeilinger, Self-cooling of a micromirror by radiation pressure, *Nature* **444**, 67 (2006).
- [32] A. Schliesser, R. Rivière, G. Anetsberger, O. Arcizet, and T. J. Kippenberg, Resolved-sideband cooling of a micromechanical oscillator, *Nat. Phys.* **4**, 415 (2008).
- [33] M. Poggio, C. L. Degen, H. J. Mamin, and D. Rugar, Feedback Cooling of a Cantilever's Fundamental Mode Below 5 mK, *Phys. Rev. Lett.* **99**, 017201(4) (2007).
- [34] T. Corbitt, Y. Chen, E. Innerhofer, H. Müller-Ebhardt, D. Ottaway, H. Rehbein, D. Sigg, S. Whitcomb, C. Wipf, and N. Mavalvala, An All-optical Trap for a Gram-scale Mirror, *Phys. Rev. Lett.* **98**, 150802(4) (2007).
- [35] T. Corbitt, C. Wipf, T. Bodiya, D. Ottaway, D. Sigg, N. Smith, S. Whitcomb, and N. Mavalvala, Optical Dilution and Feedback Cooling of a Gram-scale Oscillator to 6.9 mK, *Phys. Rev. Lett.* **99**, 160801(4) (2007).
- [36] C. M. Mow-lowry, A. J. Mullavey, S. Gobler, M. Gray, and D. E. McClelland, Cooling of a Gram-scale Cantilever Flexure to 70 mK with a Servo-modified Optical Spring, *Phys. Rev. Lett.* **100**, 010801 (2008).
- [37] A. Hines, L. Richardson, H. Wisniewski, and F. Guzman, Optomechanical Inertial Sensors, *Appl. Opt.* **59**, G167 (2020).
- [38] A. Schroeter, R. Nawrodt, R. Schnabel, S. Reid, I. W. Martin, S. Rowan, C. Schwarz, T. Koettig, R. Neubert, M. Thürk, W. Vodel, A. Tunnermann, K. Danzmann, and P. Seidel, On the mechanical quality factors of cryogenic test masses from fused silica and crystalline quartz, [ArXiv:0709.4359](https://arxiv.org/abs/0709.4359), 2007.
- [39] R. W. P. Drever, J. L. Hall, F. V. Kowalski, J. Hough, G. M. Ford, A. J. Munley, and H. Ward, Laser phase and frequency stabilization using an optical resonator, *Appl. Phys. B* **31**, 97 (1983).
- [40] D. G. Matei, T. Legero, S. Häfner, C. Grebing, R. Weyrich, W. Zhang, L. Sonderhouse, J. M. Robinson, J. Ye, F. Riehle, and U. Sterr, 1.5  $\mu\text{m}$  Lasers with Sub-10 mHz Linewidth, *Phys. Rev. Lett.* **118**, 263202 (2017).
- [41] E. D. Black, An introduction to Pound-Drever-Hall laser frequency stabilization, *Am. J. Phys.* **69**, 79 (2001).
- [42] C. Cahillane, G. L. Mansell, and D. Sigg, Laser frequency noise in next generation gravitational-wave detectors, *Opt. Express* **29**, 42144 (2021).
- [43] R. Wagner, F. Guzman, A. Chijioke, G. K. Gulati, M. Keller, and G. Shaw, Direct measurement of radiation pressure and circulating power inside a passive optical cavity, *Opt. Express* **26**, 23492 (2018).
- [44] J. Melcher, J. Stirling, F. G. Cervantes, J. R. Pratt, and G. A. Shaw, A self-calibrating optomechanical force sensor with femtonewton resolution, *Appl. Phys. Lett.* **105**, 233109 (2014).
- [45] *Digital (Sampled) Phase-lock Loops* (John Wiley and Sons, Ltd, Hoboken, USA, 2005), Chap. 13, p. 282.
- [46] C. M. Pluchar, A. R. Agrawal, E. Schenk, and D. J. Wilson, Towards cavity-free ground-state cooling of an acoustic-frequency silicon nitride membrane, *Appl. Opt.* **59**, G107 (2020).
- [47] M. Pinard, P. F. Cohadon, T. Briant, and A. Heidmann, Full mechanical characterization of a cold damped mirror, *Phys. Rev. A* **63**, 013808(12) (2000).